Structure–Curie temperature relationships in $BaTiO_3$-based ferroelectric perovskites: Anomalous behavior of (Ba,Cd)TiO_3 from DFT, statistical inference, and experiments

Prasanna V. Balachandran,[1,*] Dezhen Xue,[1,2] and Turab Lookman[1,†]

[1]*Theoretical Division, Los Alamos National Laboratory Los Alamos, New Mexico 87545, USA*

[2]*State Key Laboratory for Mechanical Behavior of Materials, Xi'an Jiaotong University, Xi'an 710049, China*

(Received 25 November 2015; revised manuscript received 17 February 2016; published 11 April 2016)

One of the key impediments to the development of $BaTiO_3$-based materials as candidates to replace toxic-Pb-based solid solutions is their relatively low ferroelectric Curie temperature (T_C). Among many potential routes that are available to modify T_C, ionic substitutions at the Ba and Ti sites remain the most common approach. Here, we perform density functional theory (DFT) calculations on a series of $ATiO_3$ and $BaBO_3$ perovskites, where A = Ba, Ca, Sr, Pb, Cd, Sn, and Mg and B = Ti, Zr, Hf, and Sn. Our objective is to study the relative role of A and B cations in impacting the T_C of the tetragonal ($P4mm$) and rhombohedral ($R3m$) ferroelectric phases in $BaTiO_3$-based solid solutions, respectively. Using symmetry-mode analysis, we obtain a quantitative description of the relative contributions of various divalent (A) and tetravalent (B) cations to the ferroelectric distortions. Our results show that Ca, Pb, Cd, Sn, and Mg have large mode amplitudes for ferroelectric distortion in the tetragonal phase relative to Ba, whereas Sr suppresses the distortions. On the other hand, Zr, Hf, and Sn tetravalent cations severely suppress the ferroelectric distortion in the rhombohedral phase relative to Ti. In addition to symmetry modes, our calculated unit-cell volume also agrees with the experimental trends. We subsequently utilize the symmetry modes and unit-cell volumes as features within a machine learning approach to learn T_C via an inference model and uncover trends that provide insights into the design of new high-T_C $BaTiO_3$-based ferroelectrics. The inference model predicts $CdTiO_3$-$BaTiO_3$ solid solutions to have a higher T_C and, therefore, we experimentally synthesized these solid solutions and measured their T_C. Although the calculated mode strength for $CdTiO_3$ in the tetragonal phase is even larger than that for $PbTiO_3$, the T_C of $CdTiO_3$-$BaTiO_3$ solid solutions in the tetragonal phase does not show any appreciable enhancement. Thus, $CdTiO_3$-$BaTiO_3$ does not follow the inference model, which is based on established data and trends for $ATiO_3$. Rather, our experimental phase diagram for $CdTiO_3$-$BaTiO_3$ suggests that it behaves markedly differently from any other $BaTiO_3$-based systems studied so far.

DOI: 10.1103/PhysRevB.93.144111

I. INTRODUCTION

$BaTiO_3$-based perovskites have attracted significant attention as a potential alternative for Pb-based functional materials in many applications as piezoelectrics, ferroelectrics, and electrocalorics. Pure $BaTiO_3$ has a complex phase diagram. It undergoes, on cooling, a series of structural phase transformations from cubic (C) → tetragonal (T) → orthorhombic (O) → rhombohedral (R) (see Fig. 1). The high-symmetry cubic structure belongs to $Pm\bar{3}m$ space group, which is centrosymmetric and, therefore, possess no piezoelectric or ferroelectric activity. On the other hand, in the three low-symmetry structures T ($P4mm$), O ($Amm2$), and R ($R3m$), the inversion symmetry is broken and $BaTiO_3$ becomes ferroelectric. In pure $BaTiO_3$, the ferroelectric Curie temperature (T_C) is experimentally measured at ∼393 K and refers to the temperature at which the C → T transition occurs on cooling [1]. Similarly, the T → O and O → R phase transformations occur at 268 and 183 K, respectively [1].

At room temperature (in the T phase), pure $BaTiO_3$ has a relatively low piezoelectric coefficient (d_{33} ∼ 200 pC/N) when compared to Pb(Zr, Ti)O_3 (PZT), whose d_{33} is 500–600 pC/N [2,3]. However, when doped, $BaTiO_3$-based systems can exhibit higher d_{33}, even surpassing that of PZT [3]. As a result, chemical substitutions at the Ba and Ti sites are common to enhance the performance of $BaTiO_3$-based functional materials. Notwithstanding a giant piezoelectric response, there are a number of technological challenges that must be met in order for these materials to be useful for applications as sensors, actuators, transducers, and transformers. For instance, there are many properties that must be optimized simultaneously, namely, the T_C, piezoelectric response, electromechanical coupling, electrical resistivity, mechanical and electrical quality factor, dielectric permittivity, and thermal stability [4,5]. The nature of application demands different figures of merit and, accordingly, appropriate materials design and selection practices are followed.

In the development of $BaTiO_3$-based materials as high-performance piezoelectrics, and a potential alternative to toxic-Pb-based functional materials, a common strategy is to mix the two end-member compositions that have a C → T and C → R phase transformation [6]. This strategy mimics that used for PZT, which remains one of the best high-performance piezoelectric materials with widespread fundamental and technological impact to date. As the relative concentrations of the two end-member chemical constituents are changed, a morphotropic phase boundary (MPB) is formed, where the $P4mm$ and $R3m$ phases become energetically degenerate [7–9]. At the MPB, the activation barrier for polarization rotation is reduced, which results in superior

*pbalachandran@lanl.gov

†txl@lanl.gov

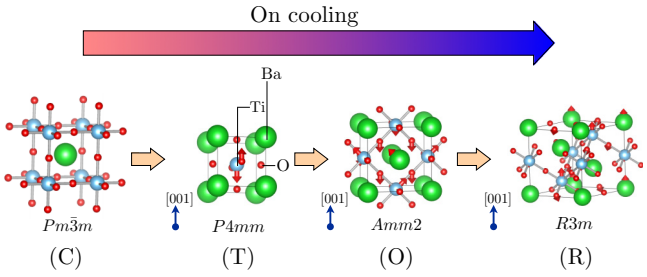

FIG. 1. Sequence of structural phase transitions in pure $BaTiO_3$ when cooled from a higher temperature (cooling direction shown). On cooling, the structure changes from cubic (C) to tetragonal (T) to orthorhombic (O) to rhombohedral (R) symmetry. Space groups (in international notation) associated with each of these phases are also given in the figure. The C phase is centrosymmetric with no piezoelectric or ferroelectric activity, whereas the T, O, and R phases are ferroelectric with broken inversion symmetry. The cooperative atomic displacements in the three ferroelectric phases relative to the high-symmetry C phase are shown using red arrows.

piezoelectric and electromechanical response for a given operating temperature range [10]. One of the canonical examples is the $Ba_{0.7}Ca_{0.3}TiO_3$ ($BC_{0.3}T$)–$BaTi_{0.8}Zr_{0.2}O_3$ ($BZ_{0.2}T$) solid solution, for which it was experimentally shown that at the MPB composition (50% $BC_{0.3}T$–50% $BZ_{0.2}T$) d_{33} is 620 pC/N, which is even higher than that of some Pb-based counterparts [3].

Normally, $BaTiO_3$ is doped at the Ba and Ti sites to construct PZT-like phase diagrams. Some of the common dopants utilized are the divalent Ca and Sr cations that substitute for the Ba site; similarly, tetravalent Zr, Hf, and Sn cations substitute for the Ti site. These dopants affect the relative phase boundaries for $C \rightarrow T \rightarrow O \rightarrow R$ transitions, which are in turn exploited to manipulate the piezoelectric properties [3,7]. For example, consider the solid solutions of $Ba_{1-x}Ca_xTiO_3$ (BCT), where x varies from 0.01 to 0.50. When x becomes greater than 0.2, the $T \rightarrow O$ and $O \rightarrow R$ transformation temperatures shift to very low values, so much so that the T phase is considered as the stable experimental ground state [11]. Similarly, in the $BaTi_{1-y}Zr_yO_3$ (BZT) solid solutions, at higher y concentrations the $C \rightarrow T$ and $T \rightarrow O$ phase boundaries disappear and only $C \rightarrow R$ transformations are experimentally observed [12]. Solid solutions of BZT and BCT contain an MPB, similar to that in the PZT system. In addition, these divalent and tetravalent dopants also affect T_C. One of the major drawbacks in the deployment of $BaTiO_3$-based piezoelectrics as Pb-free alternatives has been its relatively low T_C.

Our main goal in this paper is to study the structure–T_C relationship for $BaTiO_3$ solid solutions, with the objective of designing new high-T_C end-member compositions that are not explored in the literature. We identify this as a critical step in the development of novel high-performance $BaTiO_3$-based piezoelectric perovskites. To accomplish the objective, we develop an approach that integrates density functional theory (DFT), mode crystallography, and statistical inference with experiments to gain insights into the role of dopant cations at the Ba and Ti sites of the $BaTiO_3$ perovskite structure. We use DFT [13] to focus on the undoped $ATiO_3$ and $BaBO_3$ perovskites by constraining them in the T and R crystal symmetries, respectively, where A = Ca, Sr, Mg, Pb, Cd, Ba, and Sn and B = Ti, Zr, Hf, and Sn are divalent and tetravalent cations, respectively. We note that some of the $ATiO_3$ and $BaBO_3$ perovskites that we have explored do not have the T and R crystal symmetries as their theoretical ground-state structure (e.g., $CaTiO_3$, $BaZrO_3$, etc.). This should not affect our goal. Constraining the crystal structures in the T and R phases is an important step in our calculations because experimentally it has been shown that Sr, Ca, or Pb addition to $BaTiO_3$ stabilizes the T phase. Similarly, Zr, Hf, and Sn addition to $BaTiO_3$ stabilizes the R phase. From our calculated $ATiO_3$ and $BaBO_3$ data for the end members, we mimic the $BaTiO_3$-$ATiO_3$ (or $BaBO_3$) solid solutions. We use this simplified description as "proxy" for representing the solid solutions within the statistical inference framework. Ideally, modeling solid solutions directly from DFT for all composition ranges in a high-throughput manner would be beneficial; however, this is a nontrivial task. Instead, we calculate several features from DFT (e.g., volume and tetragonality ratio c/a) and compare them with available experimental data. We filter only those features that agree (at least qualitatively) with experimental trends and utilize them for statistical inference. For example, we find that the trend in calculated volume for the T phase agrees well with the experimental volume. In sharp contrast, the c/a does not. Therefore, we filter volume as a potential feature for inference.

The mode crystallography [14–16] component of our work takes the computed crystal structures from DFT as input and decomposes the two ferroelectric phases (T and R) into their irreducible representations (irreps) of the high-symmetry cubic (C) structure. These irreps (Γ-point instabilities denoted as Γ_4^-), which are the frozen-phonon modes, have a clear physical meaning with respect to lattice vibrations and interatomic forces that drive a phase transition [14,15]. Moreover, they quantitatively capture the cooperative atomic displacements in the low-symmetry ferroelectric phase relative to the high-symmetry cubic phase. Within the framework of Landau theory of phase transitions, these irrep-induced distortion modes serve as the order parameters in expressing the free energy of a solid [17,18]. We utilize these irreps to understand the role of each divalent and tetravalent cation in impacting the ferroelectric distortions in the $ATiO_3$ and $BaBO_3$ crystal chemistries.

In the context of statistical inference, these irreps provide a basis for describing these materials uniquely and have the potential to serve as features [19,20] for developing structure-property relationships. Therefore, we link the amplitude of Γ_4^- irreps and the DFT unit-cell volume with the experimentally measured T_C using standard machine learning methods to establish the structure–T_C relationship for known $BaTiO_3$-based ferroelectrics. In particular, we use support vector regression with a Gaussian radial basis function kernel (SVR_{RBF}) [21–24] to train an inference model (separately for T and R phases) on known materials. We then use the SVR_{RBF} regression model to predict the T_C in the T phase of $CdTiO_3$-$BaTiO_3$ solid solutions, which has received very little attention in the literature [25].

To validate our $CdTiO_3$-$BaTiO_3$ predictions, we experimentally synthesized $Ba_{1-z}Cd_zTiO_3$ and measured its T_C, where z

varies from 0.02–0.25. We find that at room temperature the T phase is stabilized, but intriguingly the T_C (and temperatures of other structural transitions that occur on further cooling) of the solid solution remains unaffected from that of the pure $BaTiO_3$, until $z = 0.25$ (the limit to which our experiments were carried out). This is an interesting finding because the relative mode amplitude of pure $CdTiO_3$ in the tetragonal phase from our DFT calculations is even greater than that for pure $PbTiO_3$. If the well-known T_C–δ relationship suggested by Abrahams *et al.* [26] is obeyed, where δ is the displacement developed by the homopolar metal atom, then T_C is expected to increase for the $Ba_{1-z}Cd_zTiO_3$ solid solution. This is also the prediction from our statistical inference model, which is based on the trends seen in existing data and does not include any data point from $Ba_{1-z}Cd_zTiO_3$. However, we do not observe this trend in our experiments, which suggest that $CdTiO_3$-$BaTiO_3$ solid solutions behave differently from $SrTiO_3$-$BaTiO_3$, $PbTiO_3$-$BaTiO_3$, and $CaTiO_3$-$BaTiO_3$.

II. METHODS

A. Density functional theory

DFT calculations were performed within the generalized gradient approximation (GGA) PBEsol exchange-correlation functional [27] as implemented in QUANTUM ESPRESSO (QE) [28]. The core and valence electrons were treated with the ultrasoft pseudopotential [29]. To yield optimally smooth pseudopotentials, we used the Troullier-Martins pseudization method [30]. The scalar relativistic pseudopotentials were generated using the ATOMIC package [28] with the inclusion of nonlinear core corrections. The Brillouin zone integration was performed over an $8\times8\times8$ Monkhorst-Pack k-point mesh [31] centered at Γ and 60 Ry plane-wave cutoff. The atomic positions and the cell volume were allowed to change until an energy convergence threshold of 10^{-8} eV and the Hellmann-Feynman forces less than 2 meV/Å, respectively, were achieved. The crystal symmetries of the optimized structures were determined using FINDSYM [32] and the symmetry-mode analyses were performed using ISODISTORT [14]. The displacement vectors were generated using AMPLIMODES [15] and visualized in VESTA [33]. We performed phonon calculations using density functional perturbation theory (DFPT) [34] and the frozen-phonon method [35] for $BaZrO_3$, $BaHfO_3$, and $BaSnO_3$ compounds.We used the $6\times6\times6$ unshifted Monkhorst-Pack grid for the DFPT calculations with more stringent convergence criterion and imposed acoustic sum rule (simple) to the dynamical matrix to correct for the nonzero frequencies. For the frozen-phonon method we used a $2\times2\times2$ supercell. Interatomic forces from QE were used as input to PHONOPY [36] to calculate the dynamical matrices and phonon frequencies.

B. Statistical inference

We used ϵ-support vector regression with nonlinear Gaussian radial basis function kernel (SVR_{RBF}) as implemented in the e1071 package [37] in the RSTUDIO environment [38]. Mathematical background of ϵ-SVR is given in the Supplemental Material [24]. The Γ_4^- irreps from symmetry-mode analysis and unit-cell volume from DFT optimized structures serve as the feature set for predicting T_C. The hyperparameters for the SVR_{RBF} were optimized using 10-fold cross validation. Error bars for each prediction were estimated following the bootstrap resampling method in statistics [39], where 50 different samples were drawn with replacement from our data set and, concomitantly, 50 SVR_{RBF} models were trained (one model for each bootstrap sample). It is assumed that these samples are taken from or are representative of the population from which the data come from. We then use those SVR_{RBF} models to predict the T_C of compounds in the compiled data set. From 50 SVR_{RBF} models we have 50 predicted T_C values for each compound. The mean and standard deviation (error bar) estimated from those 50 predictions provide an account for model performance, which we visualize by plotting the predicted *versus* experimentally measured T_C data. We also independently tested the predictive power by leaving out two compounds, $Sr_{0.9}Sn_{0.1}TiO_3$ and $Ba_{0.82}Ca_{0.13}Sn_{0.05}TiO_3$, which were not included for training the SVR_{RBF} models but their T_C's are known from the literature.

C. Experiment

$Ba_{1-z}Cd_zTiO_3$ ($0 \leqslant z \leqslant 0.25$) ceramics were fabricated by conventional solid-state method with the raw materials of $BaCO_3$ (99.8%), CdO (99%), and TiO_2 (99.9%). The calcination was performed at 1200 °C for 3 h, and sintering was done at 1400 °C for 3 h in air. The sintered samples for dielectric and ferroelectric measurements were polished to obtain parallel sides and painted with silver electrodes. The dielectric permittivity was evaluated using a HIOKI3532 LCR meter at different frequencies (0.1, 1, 10, and 100 kHz) as a function of temperature.These measurements were used to determine the T_C of the ceramic (along with other structural transformations that are occurring at lower temperatures). We compared this T_C with the SVR_{RBF} predictions to validate our inference models. Finally, we plot temperature as a function z (i.e., Cd concentration) to map the experimental phase diagram of $Ba_{1-z}Cd_zTiO_3$.

III. FEATURE CONSTRUCTION AND ASSUMPTIONS

We consider solid solutions of $BaTiO_3$ for which experimental T_C data exist in the literature. We define each chemical composition of the solid solution by constructing linear combinations of the features based on the assumption that these linear combinations mimic the "average" behavior of the solid solution. For example, the unit-cell volume (V) for the T phase of $Ba_{1-x}Ca_xTiO_3$ (where $0 \leqslant x \leqslant 1$) is constructed in the following manner: $(1-x)V^{T}_{BaTiO_3} + (x)V^{T}_{CaTiO_3}$, where $V^{T}_{BaTiO_3}$ and $V^{T}_{CaTiO_3}$ are the unit-cell volumes of pure $BaTiO_3$ and $CaTiO_3$, respectively, in the T phase as obtained from DFT calculations. We chose only those values of x for which experimental data are available. A similar procedure was followed to construct the Γ_4^- mode amplitude feature.

The reasons and the underlying assumptions for choosing unit-cell volume and Γ-point modes as the minimal set of features describing average behavior in our data-driven modeling include the following: (i) Their simplicity, as they are readily accessible from DFT calculations and mode crystallography. (ii) We are primarily interested in the T_C of "polar" T and R phases, where the Γ_4^- mode is the order

TABLE I. Symmetry-mode analysis: unit-cell parameters for the T phase, energetics, and theoretical ground-state crystal symmetry for $ATiO_3$ compounds from DFT using PBEsol exchange-correlation functional. Amplitudes represent the mode strength in unit Å (angstrom) of irrep Γ_4^- with OPD order-parameter direction (a). a and c are the in-plane and out-of-plane lattice constants, respectively. c/a is the tetragonality ratio and ΔE is the energy difference per formula unit between the theoretical ground state and the T phase. $\Delta E = +$sign indicates that T phase is not the ground state, whereas T phase is the theoretical ground-state configuration when $\Delta E = 0$.

$ATiO_3$	Mode amplitude in Å	Volume in Å^3	a in Å	c in Å	c/a	ΔE (meV/f.u.)	Theoretical ground state
$BaTiO_3$	0.266 74	63.63	3.963 15	4.051 32	1.0222	6.5	$R3m$
$CaTiO_3$	0.505 88	58.17	3.806 19	4.015 04	1.0549	282.6	$Pnma$
$SrTiO_3$	0.104 18	59.05	3.890 59	3.901 29	1.0028	7.0	$I4/mcm$
$PbTiO_3$	0.540 24	62.60	3.878 88	4.160 80	1.0727	0	$P4mm$
$CdTiO_3$	0.619 80	59.27	3.793 21	4.119 33	1.0860	758.7	$Pna2_1$
$SnTiO_3$	0.835 58	64.41	3.798 33	4.464 77	1.1755	0	$P4mm$
$MgTiO_3$	1.047 11	60.85	3.686 49	4.477 69	1.2146	874.3	$Pnma$
$BaTiO_3$ (experimental) [49]	0.240 57	64.2816	3.999 80	4.018 02	1.0046		

parameter. Therefore, Γ-point modes were assumed to be important for our problem. The importance of unit-cell volume for ferroelectricity in perovskites is well documented in the literature [11,40–42]. (iii) We found good agreement in trends between our calculated features and experimental data. We also explored other features, such as c/a, but trends from our calculations did not agree with experiments. Therefore, unit-cell volume and Γ-point mode were considered sufficient to capture the global trend in the T_C data. (iv) They also provide a reasonable physical basis for establishing structure–T_C relationships. The fourth criterion is substantiated by the Abrahams-Kurtz-Jamieson theory for displacive ferroelectrics [26] that relates atomic displacements of homopolar atoms to T_C. Our objective was to leverage this theory (albeit in an empirical manner) by utilizing mode crystallography that goes beyond the homopolar atom displacements description. (v) We also assumed that linear mixing of the features is not an oversimplification to capture the average behavior of $BaTiO_3$ solid solutions.

IV. RESULTS AND DISCUSSION

In Tables I and II, we show the results from the symmetry-mode analysis for the C → T and C → R transitions, respectively. Experimental data from the literature are also included for comparison. Note that both the C → T and C → R phase transformations can be described by the Γ_4^- irreducible representation (irrep) [43]. However, the key difference lies in the order-parameter directions (OPDs); the OPDs for C → T and C → R transitions are one-dimensional and three-dimensional vectors, respectively. They, in turn, correspond to cooperative displacements of atoms along the [001] and [111] directions of the aristotype (high-symmetry) C phase.

A. Crystal structures from DFT-GGA (PBEsol) calculations

Since our focus is on the solid solutions of $BaTiO_3$ at the T and R ends, we use the Γ_4^- mode amplitudes of pure $BaTiO_3$ as a reference point and compare other perovskites relative to this value. In our calculations, we relaxed both the cell geometry and internal coordinates (see Sec. II A for additional details). Among all divalent cations that we have considered, only $PbTiO_3$ [44] and $SnTiO_3$ [45] have T phase as the theoretical ground-state configuration, albeit there have been experimental difficulties in the synthesis of pure $SnTiO_3$ in the perovskite crystal structure. The ground-state structures for $MgTiO_3$ [46], $CaTiO_3$ [47], $CdTiO_3$ [47], and $SrTiO_3$ [48] are $Pnma$, $Pnma$, $Pna2_1$, and $I4/mcm$, respectively. In Table I, we also give the total energy difference (ΔE) between the ground-state structure and the T phase for the $ATiO_3$ perovskites. In terms of the lattice constants and cell volume for $BaTiO_3$, our DFT-GGA (PBEsol) calculation underestimates and overestimates the a and c lattice constants, respectively, relative to the experimental data [49] (see Table I). We have also given the lattice constants and cell volume for the other $ATiO_3$ perovskites in the T phase.

Similarly, lattice constants and unit-cell volumes for the R-phase perovskites are given in Table II. Our calculated cell

TABLE II. Symmetry-mode analysis: unit-cell parameters for the R phase, energetics, and theoretical ground-state crystal symmetry for $BaBO_3$ compounds from DFT using PBEsol exchange-correlation functional. Amplitudes represent the mode strength in unit Å (angstrom) of irrep Γ_4^- with OPD order-parameter direction (a,a,a). a and c are the in-plane and out-of-plane lattice constants, respectively. ΔE is the energy difference per formula unit between the theoretical ground state and the R phase. $\Delta E = +$sign indicates that R phase is not the ground state, whereas R phase is the theoretical ground state when $\Delta E = 0$.

$BaBO_3$	Mode amplitude in Å	Volume in Å^3	a in Å	c in Å	ΔE (meV/f.u.)	Theoretical ground state
$BaTiO_3$	0.310 53	191.53	5.645 77	6.938 42	0	$R3m$
$BaZrO_3$	0.000 26	221.93	5.936 87	7.270 45	4.6	$P1$
$BaHfO_3$	0.000 24	213.62	5.861 79	7.178 77	0.16	$Pm\bar{3}m$
$BaSnO_3$	0.000 00	213.73	5.862 88	7.179 92	4.6	$P1$
$BaTiO_3$ (experimental) [50]	0.329 10	192.142	5.650 86	6.948 05		

geometry for $BaTiO_3$ in the R phase agrees well with the experimental data [50]. Note that the experimental ground state for $BaZrO_3$ [51], $BaHfO_3$ [52], and $BaSnO_3$ [53] is considered to be cubic. However, our phonon calculations show dynamical instabilities (phonons with imaginary frequencies) for $BaZrO_3$ and $BaSnO_3$. In our DFPT calculations for $BaZrO_3$, instabilities were found at the R point of the Brillouin zone [Fig. 2(a)], in good agreement with the existing literature [54,55]. However, our calculations do not agree with the DFPT work of Bilić and Gale [56], who found phonon instabilities at the M point (in addition to the R point). On the other hand, in our frozen-phonon calculations (phonon dispersion curves given in the Supplemental Material [24]), instabilities were found at the X and R points of the Brillouin zone. The origin of the X-point instability is unclear and may be due to the inherent limitations of the frozen-phonon method. We "froze-in" the real-space eigendisplacements of unstable phonon modes at the X and R points and performed full structural relaxation (atom positions and lattice) in the $Pmmm$ and $P1$ crystal symmetries, respectively. The ground-state structure was determined to be the $P1$ space group [Fig. 2(d)], where the out-of-phase octahedral rotations [that transform as irrep R_4^+ with OPD (a,b,c) [57,58]] stabilize the triclinic symmetry.

We then performed symmetry-mode analysis for the ground state $P1$ structure. In addition to R_4^+, we also found contributions from displacements described by irrep X_4^-. The mode amplitude (or strength) of X_4^- was, however, substantially small compared to that of the R_4^+ irrep. The inclusion of X_4^- is important because the action of R_4^+ alone gives rise to incorrect $P\bar{1}$ symmetry. Therefore, it is the coupling $R_4^+ \oplus X_4^-$ that stabilizes the $P1$ triclinic symmetry in $BaZrO_3$ in our calculations. See Table 1 in the Supplemental Material for total energy data of different crystal symmetries [24]. In the case of $BaSnO_3$, both DFPT [Fig. 2(b)] and frozen-phonon calculations [24] found instabilities only at the R point. The ground-state structure for $BaSnO_3$ was also determined to have $P1$ triclinic symmetry (see Table 1 in the Supplemental Material [24]). But, in both $BaZrO_3$ and $BaSnO_3$ compounds, the energy difference (ΔE) between the ground state $P1$ and the cubic $Pm\bar{3}m$ structures was only of the order of a few meV, which could be one of the reasons for not observing these

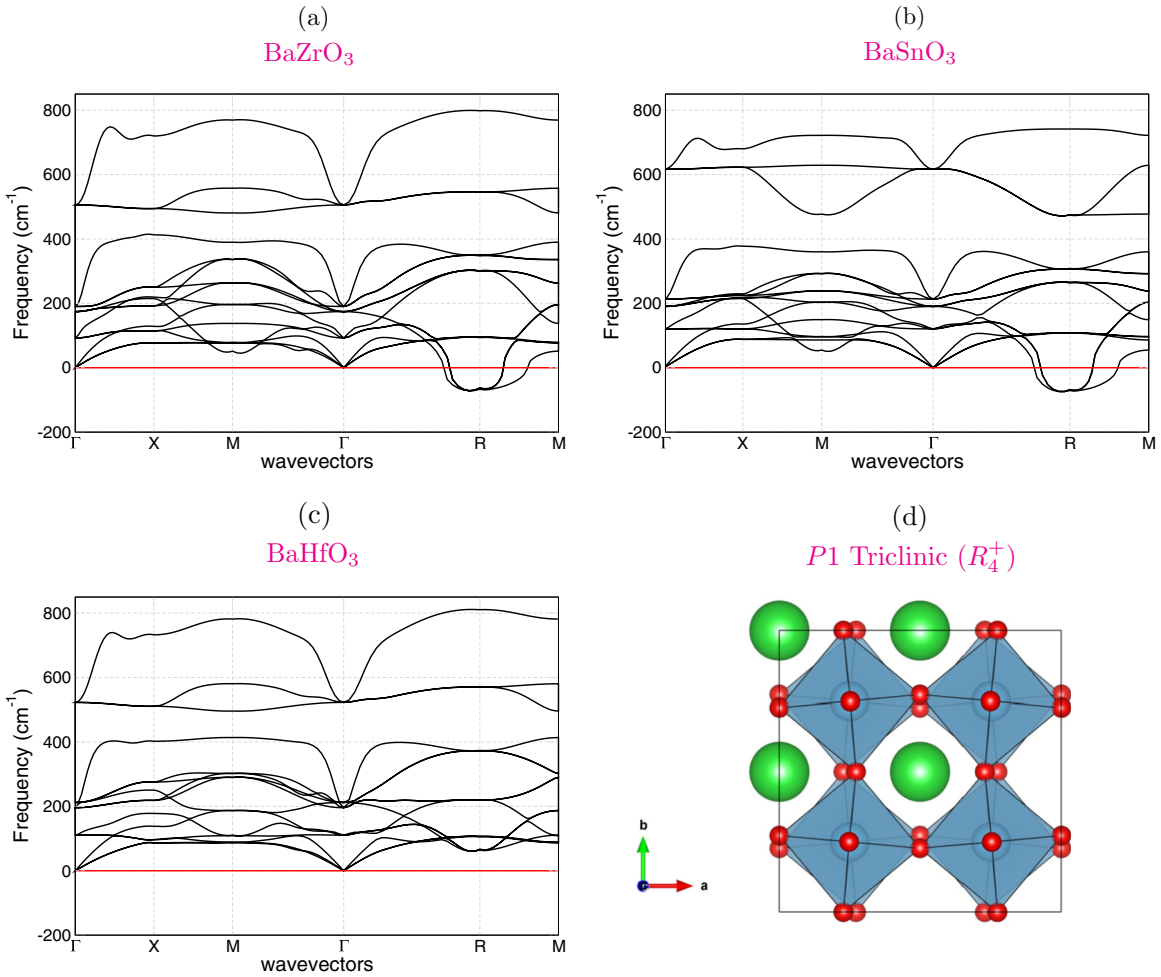

FIG. 2. Phonon band structures for (a) $BaZrO_3$, (b) $BaSnO_3$, and (c) $BaHfO_3$ from the DFPT calculations using PBEsol functional. Phonon instabilities were found in the $BaZrO_3$ and $BaSnO_3$ perovskites, whereas the theoretical ground state is determined to be cubic for $BaHfO_3$. In (d) the crystal structure of ground state $P1$ symmetry for $BaZrO_3$ and $BaSnO_3$ is shown. Out-of-phase octahedral rotations are described by the irrep R_4^+ (R-point instability).

low-symmetry structures in bulk ceramics. Recent terahertz time-domain spectroscopy (THz-TDS) has found evidence for a low-symmetry triclinic phase in single crystal $BaZrO_3$ [59], whereas no such data exist for $BaSnO_3$ to validate our DFPT and frozen-phonon calculations. In sharp contrast, no phonon instabilities were found in the $BaHfO_3$ system from both DFPT [Fig. 2(c)] and frozen-phonon methods [24], indicating that its theoretical ground-state structure is cubic.

B. Symmetry-mode analysis

From the DFT data given in Table I, we find that all divalent cations, except Sr^{2+}, have a relatively large amplitude for Γ_4^- irrep in the T phase compared to $BaTiO_3$. Compound $MgTiO_3$ has the largest value for Γ_4^- in the T phase, but it is known from previous work that the ground state of $MgTiO_3$ is *Pnma* and, furthermore, it is challenging to stabilize a pure perovskite phase in $MgTiO_3$ at ambient conditions due to the relatively smaller ionic size of Mg^{2+} cation [60]. As noted earlier, among all divalent cations that we have explored, only $PbTiO_3$ and $SnTiO_3$ have T phase as the theoretical ground state.

On the other hand, large differences in the amplitudes of the irreps are noticeable in our DFT calculations for the $BaBO_3$ end members in the R phase (see Table II). The mode amplitude for $BaTiO_3$ is estimated as 0.310 53 Å, which compares favorably with the experimental value of 0.3291 Å. However, the mode amplitude is found to be nearly zero for $BaZrO_3$, $BaHfO_3$, and $BaSnO_3$ in the R phase. These results indicate that the $BaZrO_3$, $BaHfO_3$, and $BaSnO_3$ systems strongly resist rhombohedral distortions, but prefer cubic symmetry (in good agreement with the experimental observations in the literature and our calculated ΔE value from DFT).

As noted before in Sec. III, instead of directly modeling the solid solutions from DFT, we consider only the end-member compositions ($ATiO_3$ or $BaBO_3$) and interpolate between them. We thus linearly combine the irreps based on the assumption that the solid solution mimics the average behavior of the two end members, which has been applied in the past to model the solid-solution behavior of $PbTiO_3$ systems [43]. We checked the validity of our assumption for Pb-free compounds by comparing the DFT results to the experimental data (where available). This is shown in Fig. 3. Note that we were only able to find limited experimental crystal structure data for the solid solutions of $BaTiO_3$-$SrTiO_3$ [61], $BaTiO_3$-$CaTiO_3$ [62], and $Ba_{0.79}Ca_{0.16}Sn_{0.05}TiO_3$ [63] in the T phase. Data for other solid solutions are not shown because there were no experimental data for comparison in the International Crystal Structure Database (ICSD) repository [64] or published literature.

For the $BaTiO_3$-$SrTiO_3$ solid solution [Fig. 3(a)], we find a negative slope of magnitude 0.1626 indicating that the addition of Sr to $BaTiO_3$ decreases the mode amplitude. In the same plot, we also show the experimental data (open circle) and find that the mode amplitude first decreases and then increases. The physical origin of this apparent increase is unclear and its validity is difficult to confirm due to the absence of other independent experimental measurements. In $BaTiO_3$-$CaTiO_3$ [Fig. 3(b)], we find a positive slope of magnitude 0.2391. One experimental data point for $Ba_{0.88}Ca_{0.12}TiO_3$ in the T phase also shows an increased value of mode amplitude relative to pure $BaTiO_3$, indicating agreement with our DFT data. Finally,

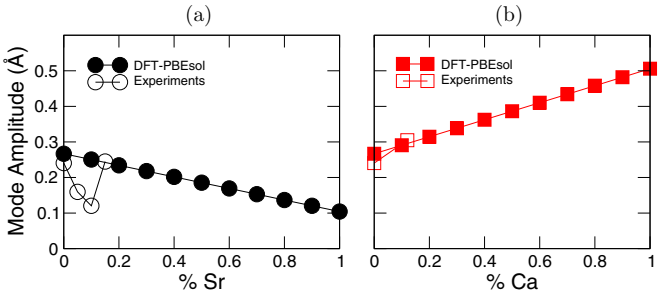

FIG. 3. Mode amplitudes (in Å) as a function of chemical composition of the solid solution in the T phase for (a) (Ba,Sr)TiO_3 and (b) (Ba,Ca)TiO_3. Filled and open symbols represent data from theoretical DFT-PBEsol calculations and experimental measurements in the literature [61,62], respectively. The end-member mode amplitudes (at weight fractions 0% and 1%) were obtained directly from DFT-PBEsol calculations. Linear mixing rule was used to calculate the theoretical mode amplitudes in the solid solutions.

for $Ba_{0.79}Ca_{0.16}Sn_{0.05}TiO_3$, the experimental [63] and our DFT values for irrep Γ_4^- are 0.1187 and 0.333 44 Å, respectively. Our calculated Γ_4^- for this compound did not agree with the experimental result.

On the other hand, in terms of unit-cell parameters, the c/a trend is not in agreement. Within our linear interpolation constraint, we anticipate c/a to increase with Ca addition (see Table I); the c/a for $CaTiO_3$ is 1.0549, which is greater than that of $BaTiO_3$ (1.0222). However, intriguingly, it has been experimentally shown that c/a decreases with increasing Ca content [65]. In contrast, the unit-cell volume is experimentally shown to decrease with increasing Ca content, which agrees with our DFT calculations (see Table I). Therefore, with cautious optimism, we consider our DFT data to be valid for further considerations and feature development. The key outcome of this comparison exercise between the experimental and our DFT data is the identification of *two key features* that we use for our machine learning, namely, (i) Γ_4^- mode amplitudes from the symmetry-mode analysis and (ii) unit-cell volume. *Can we use these two features to capture the trend of T_C in $BaTiO_3$-based ferroelectrics with an inference model and demonstrate its predictive ability?* We address these questions in the ensuing sections.

C. Trends in T_C from literature

In the literature, experimental T_C data exist for the following solid solutions: $PbTiO_3$-$BaTiO_3$, $SrTiO_3$-$BaTiO_3$, $CaTiO_3$-$BaTiO_3$, $BaZrO_3$-$BaTiO_3$, $BaHfO_3$-$BaTiO_3$, and $BaSnO_3$-$BaTiO_3$ [66]. In Fig. 4, we show how T_C changes in $BaTiO_3$ solid solutions (data taken from previously published experimental results [66]). Addition of $SrTiO_3$ and $PbTiO_3$ decreases and increases the T_C of $BaTiO_3$, respectively, for the T phase. In sharp contrast, addition of $CaTiO_3$ has only a marginal effect on the T_C of the T phase. Furthermore, $CaTiO_3$ addition also suppresses the stability field of O and R phases. In the case of $BaZrO_3$, $BaHfO_3$, and $BaSnO_3$, the stability field of T and O phases is suppressed, whereas the R-phase region is significantly enhanced. Addition of $BaZrO_3$, $BaHfO_3$, and $BaSnO_3$ also severely reduces the T_C; here, T_C corresponds to transition between the paraelectric C and the ferroelectric

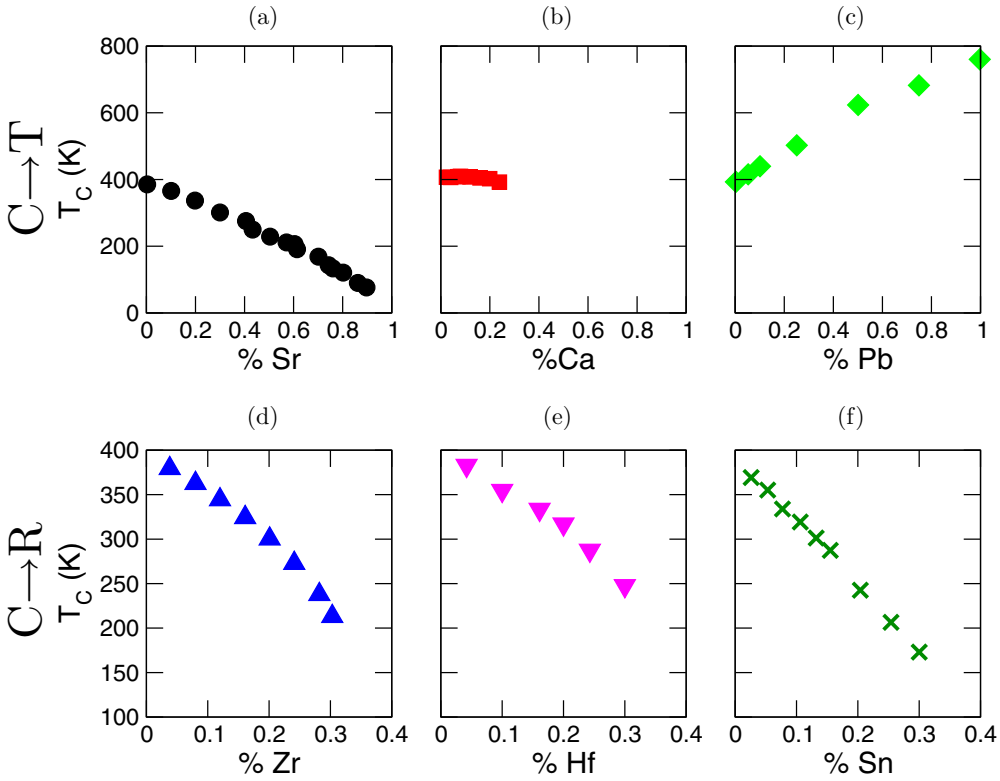

FIG. 4. (a)–(c) Experimental T_C trends for the T phase ($P4mm$ crystal symmetry) for $BaTiO_3$-$ATiO_3$ solid solutions, where A = Sr (black circle), Ca (red squares), and Pb (green diamond). (d)–(f) Experimental T_C trends for the R phase ($R3m$ crystal symmetry) for $BaTiO_3$-$BaBO_3$ solid solutions, where B = Zr (blue triangle up), Hf (magenta triangle down), and Sn (dark green cross sign).

R phase. In terms of data set size for statistical inference, we compiled a total of 31 and 23 unique chemical compositions belonging to T and R phases, respectively.

D. Predictive design via informatics

Abrahams *et al.* [26], originally, formulated one of the well-known relationships linking atomic displacements to T_C. According to their work, for a displacive ferroelectric phase transition, $T_C \propto \delta^2$, where δ is the displacement of the homopolar atom. They validated this relationship for some of the well-known simple ferroelectric systems, such as $PbTiO_3$ and $BaTiO_3$. Since this early work, a number of refinements have been suggested to their model, which incorporate complexities of atomic displacements arising from more than one ion in the solid solutions (e.g., $PbTiO_3$-based solid solutions [67]) and inclusion of higher-order terms in the atomic displacements (up to 12th polynomial order for pure $PbTiO_3$) [68]. However, no such theoretical modeling has been demonstrated for $BaTiO_3$-based solid solutions. Therefore, no predictive theories exist for modeling the behavior of T_C in $BaTiO_3$-based solid solutions. Recently, Heitmann-Rossetti [8] and Acosta *et al.* [9] have shown the potential of Landau theory in modeling the thermodynamics of $BaTiO_3$-based solid solutions. However, accelerated inverse design of new material chemistries with targeted properties using Landau theory is a nontrivial task. It requires *a priori* knowledge of how parameters are related to materials that have not been experimentally synthesized or characterized.

We explore in this paper a data-driven informatics-based approach for predicting the T_C of $BaTiO_3$-based solid solutions, which is attracting significant attention in the literature where predictive theories are prohibitive or nonexistent. We employ Γ_4^- mode amplitudes and unit-cell volume as features and the goal is to use them to predict the T_C of $BaTiO_3$ solid solutions. We utilize support vector regression with a radial-basis function (SVR_{RBF}) as the kernel for the regression problem (additional details given in Sec. II B and Supplemental Material [24]). We build separate regression models for the T and R phases. Experimental T_C data for $PbTiO_3$-$BaTiO_3$, $SrTiO_3$-$BaTiO_3$, $CaTiO_3$-$BaTiO_3$, $BaZrO_3$-$BaTiO_3$, $BaHfO_3$-$BaTiO_3$, and $BaSnO_3$-$BaTiO_3$ solid solutions serve as the data set for the informatics approach. We constructed two data sets, one for the T phase and the other for the R phase. There were 31 and 23 data points for training the T_C SVR_{RBF} model for the T and R phases, respectively. In Figs. 5(a)–5(d), we show results from the SVR_{RBF} model. The model performs reasonably well in capturing the behavior of T_C (see Fig. 5). Mean values for T_C and its standard deviation (error bars) were obtained from 50 different statistical bootstrap samples.

In addition to Ca, Sr, and Pb, one could also substitute Cd, Sn, and Mg in the Ba site. Among Cd, Sn, and Mg, only Cd substitution was determined to be feasible experimentally because only $CdTiO_3$ has been shown to have a pure perovskite phase [69,70]. Since chemical substitutions at the Ba site are known to stabilize the T phase, we used the SVR_{RBF} model developed for the T phase to predict the T_C for $Ba_{1-z}Cd_zTiO_3$

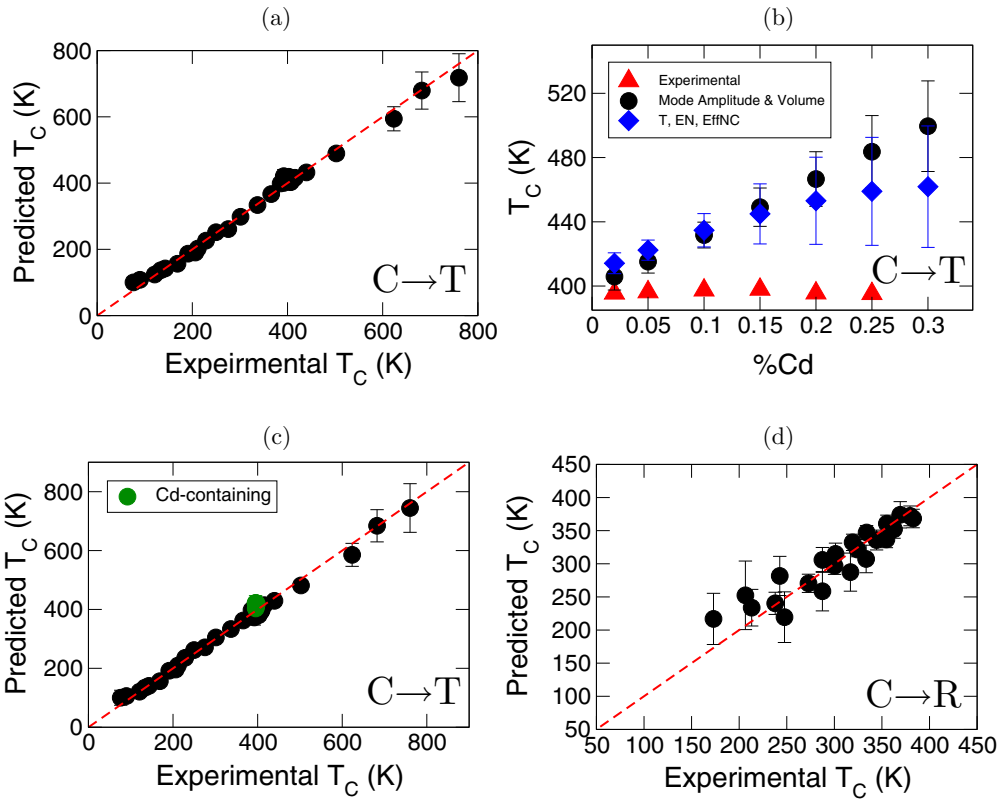

FIG. 5. (a) Predicted vs experimental T_C for the T-phase $BaTiO_3$ solid solutions. SVR_{RBF} was trained on Sr, Ca, and Pb-substituted $BaTiO_3$. (b) Comparison of experimental (filled red triangles), SVR_{RBF} predicted T_C using mode amplitude and unit-cell volume from DFT as features (filled black circles) and SVR_{RBF} predicted T_C using tolerance factor (T), Pauling electronegativity ratio of A, and Ti atoms (EN) and effective nuclear charge ratio (EffNC) of A^{2+} and Ti^{4+} cations as features (filled blue diamonds) for Cd-substituted $BaTiO_3$ in the T phase. (c) Revised SVR_{RBF} predicted vs experimental T_C for the T-phase $BaTiO_3$ solid solutions, which now also includes the Cd-substituted $BaTiO_3$ data for training. (d) SVR_{RBF} predicted vs experimental T_C for the R-phase $BaTiO_3$ solid solutions. Error bars are the standard deviations of the predicted T_C from 50 bootstrapped samples.

solid solutions. The machine learning results are shown in Fig. 5(b) (filled black circles) from which we find that the addition of Cd has a positive effect on enhancing the T_C of the $Ba_{1-z}Cd_zTiO_3$ solid solution. In addition to the Γ_4^- mode amplitude and unit-cell volume as features, we also explored some of the common crystal chemistry features [60] such as tolerance factor [71], Pauling electronegativity [72], ratio of A and Ti atoms and effective nuclear charge ratio of A^{2+} and Ti^{4+} cations (calculated as the ratio of nominal charge to squared Shannon's ionic radii [73]) to predict the T_C. The results are shown in Fig. 5(b) (filled blue diamonds). Notice that the predicted trend remains the same for both the feature sets, i.e., T_C increases as % Cd increases, indicating robustness in our predicted T_C trend.

Motivated by this finding, we experimentally synthesized $Ba_{1-z}Cd_zTiO_3$ solid solutions for $z = 0.02$, 0.05, 0.10, 0.15, 0.20, and 0.25, using the conventional powder processing method (see Sec. II C for additional details). Dielectric permittivity results for various $Ba_{1-z}Cd_zTiO_3$ are shown in Fig. 6, from which we also construct the phase diagram (shown in Fig. 7). As anticipated, the ferroelectric transition at room temperature is between the C and T phases, but intriguingly, we find that the Cd substitution does not affect the T_C of the ceramic. From Table I for the T phase, it can be seen that the unit-cell volume of $CdTiO_3$ is between $CaTiO_3$ and $PbTiO_3$, whereas the mode amplitude for $CdTiO_3$ is even greater than that of $PbTiO_3$. Note that our SVR_{RBF} machine learning model that predicts the T_C of the T phase has not used any Cd-based compounds for training.

In Fig. 5(b), we overlay the experimentally measured T_C (filled red triangles) on top of the machine learning predictions. The agreement is good only near the dilute limit ($z = 0.02$). The informatics-based SVR_{RBF} model predicts that T_C should increase with increasing Cd content. In contrast, the experimental data show that T_C increases slightly first (from 395.5 K for $z = 0.02$ to 397.9 K for $z = 0.15$), but then decreases to 395.2 K when $z = 0.25$. The discrepancy between our informatics-based model and the experimental data could (most likely) stem from the fact that our SVR_{RBF} algorithm did not have in its training set any samples showing a trend similar to $CdTiO_3$. This is one of the well-known shortcomings of the data-driven approach, i.e., extrapolation to an unknown search space. In Fig. 5(c), we augment our training data set with the Cd-containing compound and retrain the SVR_{RBF} model. The model then captures the trend in T_C for $Ba_{1-z}Cd_zTiO_3$.

The SVR_{RBF} predicted vs experimentally measured T_C for the R phase is shown in Fig. 5(d). In the case of the R phase, which requires substitution at the Ti site, a quick survey of

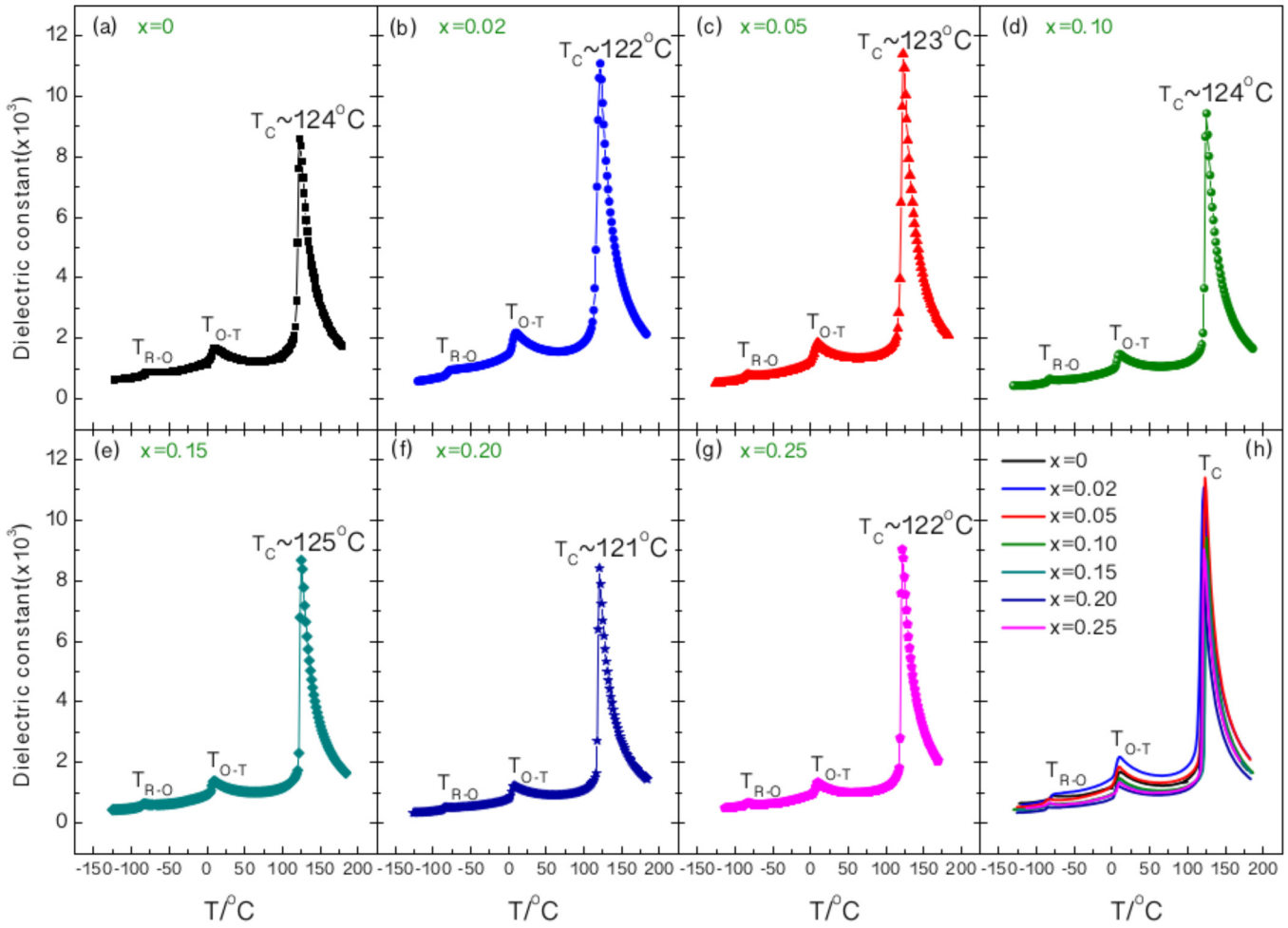

FIG. 6. (a)–(g) Dielectric permittivity measurement data as a function of temperature for $Ba_{1-z}Cd_zTiO_3$, when $z =$ (a) 0, (b) 0.02, (c) 0.05, (d) 0.10, (e) 0.15, (f) 0.20, and (g) 0.25. Different structural transitions are also identified. (h) Summary of all permittivity plots, showing that the concentration of Cd (i.e., z) has little effect on the transition temperatures.

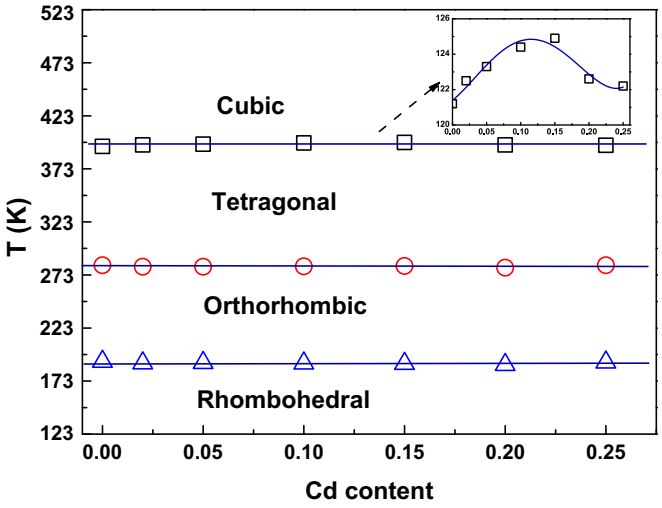

FIG. 7. Phase diagram of $Ba_{1-z}Cd_zTiO_3$, where $z \leqslant 0.25$. In contrast to other known $BaTiO_3$ solid solutions, the structural transition temperatures remain essentially unaffected in the explored Cd-concentration range.

the periodic table suggests the following cations: Fe^{4+}, Mn^{4+}, Co^{4+}, Ru^{4+}, Ir^{4+}, or Rh^{4+} (to name a few) that have partial d-orbital occupancy and therefore, electron correlation, which we do not consider in this work. Therefore, we do not predict any new $BaBO_3$-based system. Nevertheless, our work shows that the Γ_4^- mode amplitude and unit-cell volume serve as good features for data-driven modeling of $BaTiO_3$-based materials.

V. PREDICTIVE POWER

Given that our SVR_{RBF} models failed to accurately predict the T_C of $Ba_{1-z}Cd_zTiO_3$, it is reasonable to ask the following question: *Is our approach indeed good for making accurate predictions?* We address this by predicting the T_C's of two compounds: $Sr_{0.9}Sn_{0.1}TiO_3$ [74] and $Ba_{0.82}Ca_{0.13}Sn_{0.05}TiO_3$ [75], which were not used for training the SVR_{RBF} models. These compounds are shown to undergo a C → T phase transition on cooling [75] with experimentally measured T_C's equal to ∼200 and 428 K, respectively. Also, note that none of our training data included Sn^{2+} at the Ba site. Therefore, these compounds serve as an ideal test set for

TABLE III. Predictive power of SVR_{RBF} models on the independent test set. Prediction uncertainties are the standard deviation of the predicted T_C from 50 SVR_{RBF} models.

Compound	T_C (in K) from experiments [74,75]	T_C (in K) predicted from SVR_{RBF} that did not include Cd compounds	T_C (in K) predicted from SVR_{RBF} that included Cd compounds
$Sr_{0.9}Sn_{0.1}TiO_3$	~200	118.8 ± 18.74	170.4 ± 99.16
$Ba_{0.82}Ca_{0.13}Sn_{0.05}TiO_3$	428	458.6 ± 13.44	426.7 ± 12.07

evaluating our models. In Table III we show the predictions along with uncertainties. Interestingly, the SVR_{RBF} models that contained Cd compounds in the training set performed much better in predicting T_C than those that did not. This exercise shows that our SVR_{RBF} model has *learned* from the $Ba_{1-z}Cd_zTiO_3$ data and *adapted* to make reliable predictions.

In Fig. 8, we show the fitness landscape of the predicted T_C in the form of a contour plot for the T phase and show how it changes before and after including the $Ba_{1-z}Cd_zTiO_3$ data. We setup a uniform grid with 25 551 data points that span our feature space, where unit-cell volume and Γ_4^- mode amplitude were varied in the range 59–64 and 0.1–0.6, respectively, and we applied the SVR_{RBF} models to predict the T_C at each of those points. Feature data along with SVR_{RBF} predictions and uncertainties are given in the Supplemental Material [24]. In Figs. 8(a) and 8(b), we show the predicted T_C before and after retraining with the new $Ba_{1-z}Cd_zTiO_3$ data, respectively, when both unit-cell volume and Γ_4^- mode amplitude features take small values. Augmentation of $Ba_{1-z}Cd_zTiO_3$ data changed the SVR_{RBF} fitness landscape suggesting that it contained new information that was originally not found in the $CaTiO_3$, $SrTiO_3$, or $PbTiO_3$-$BaTiO_3$ solid solutions. We find support for this conclusion in our experimental phase diagram for the Cd-$BaTiO_3$ solid solution, which is shown in Fig. 7. This phase diagram is markedly different from those that are known so far. The ramifications of including $Ba_{1-z}Cd_zTiO_3$ can also be seen in our predictions for $Sr_{0.9}Sn_{0.1}TiO_3$ (Table III), where our retrained SVR_{RBF} models performed relatively well compared to the original one. Similarly, in Figs. 8(c) and 8(d) we plot the predicted T_C at the other extreme, where unit-cell volume and Γ_4^- mode amplitude take large values. Notice the large difference in the predicted T_C scales. Even though the predicted T_C shows a significant increase in Fig. 8(d) [relative to Fig. 8(c)], there were also large uncertainties in that feature space (see Supplemental Material). As a result, we anticipate this landscape to evolve as new chemistries are explored and more experiments are performed.

VI. SUMMARY

Engineering the ferroelectric properties of $BaTiO_3$-based materials has key implications for the the development of

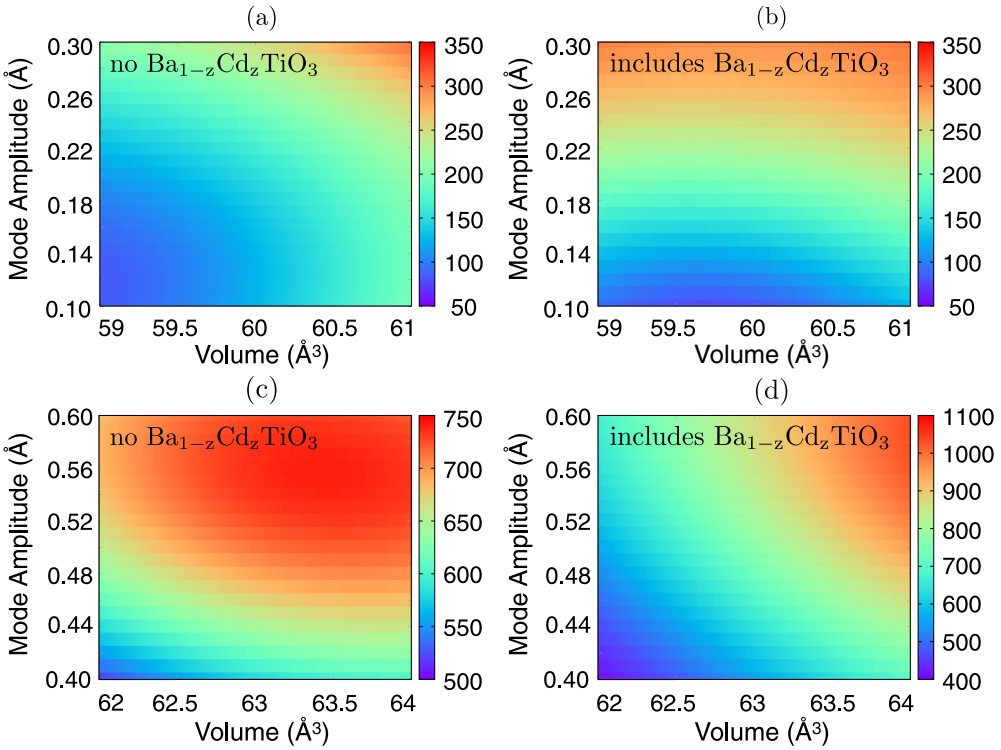

FIG. 8. Contour plots showing the predicted T_C (in K) from SVR_{RBF} models as a function of unit-cell volume (x axis) and mode amplitude (y axis). In (a) and (b) we choose the same values for volume and mode amplitudes features, but use SVR_{RBF} models that were trained without and with $Ba_{1-z}Cd_zTiO_3$ data, respectively. Similarly, in (c) and (d) we show the predicted T_C but for different ranges of volume and mode amplitude features. Notice the striking difference in the predicted T_C scales between (c) 500–750 K and (d) 400–1100 K.

Pb-free functional materials. In this work, we showed how DFT, mode crystallography, statistical inference, and experiments can be synergistically integrated to study their structure–T_C relationships. One of our key computational outcomes is the identification of irrep-induced distortion modes and unit-cell volume as important features for data-driven modeling of functional responses. With these features, we predict the T_C for $Ba_{1-z}Cd_zTiO_3$ solid solutions, however, our predictions, based on the trend shown by existing solid-solution data, do not agree with preliminary experimental results. Our experimentally determined phase diagram shows that $Ba_{1-z}Cd_zTiO_3$ is fundamentally different from any of the $BaTiO_3$-based solid solution studied so far, which is consistent with the discrepancy between our machine learning findings and experiments. At room temperature, we obtain the T phase, which could have potential implications in the design of high-performance Cd-substituted $BaTiO_3$ piezoelectrics. Our work serves as a basis to motivate further studies of experiments, computations, and theory to describe the observed trends in the unusual $Ba_{1-z}Cd_zTiO_3$ solid solution. Our work also critically brings out the cautionary tale of data-driven modeling in materials science problems and the need for incorporating adaptive design into its framework with feedback from experiments (or computations) [76,77], especially in the context of small data problems such as those addressed in this work.

ACKNOWLEDGMENTS

P.V.B., X.D., and T.L. acknowledge funding support from the Los Alamos National Laboratory (LANL) Laboratory Directed Research and Development (LDRD) DR (Grant No. 20140013DR) on Materials Informatics. The computational work made use of Institutional Computing (IC) resources at LANL.

[1] H. F. Kay and P. Vousden, London, Edinburgh, Dublin Philos. Mag. J. Sci. **40**, 1019 (1949).
[2] G. H. Haertling, J. Am. Ceram. Soc. **82**, 797 (1999).
[3] W. Liu and X. Ren, Phys. Rev. Lett. **103**, 257602 (2009).
[4] W. Heywang and H. Thomann, Annu. Rev. Mater. Sci. **14**, 27 (1984).
[5] S. Zhang and F. Yu, J. Am. Ceram. Soc. **94**, 3153 (2011).
[6] J. Rödel, W. Jo, K. T. P. Seifert, E.-M. Anton, T. Granzow, and D. Damjanovic, J. Am. Ceram. Soc. **92**, 1153 (2009).
[7] D. Xue, Y. Zhou, H. Bao, C. Zhou, J. Gao, and X. Ren, J. Appl. Phys. **109**, 054110 (2011).
[8] A. A. Heitmann and G. A. Rossetti, J. Am. Ceram. Soc. **97**, 1661 (2014).
[9] M. Acosta, N. Khakpash, T. Someya, N. Novak, W. Jo, H. Nagata, G. A. Rossetti, and J. Rödel, Phys. Rev. B **91**, 104108 (2015).
[10] M. Porta and T. Lookman, Phys. Rev. B **83**, 174108 (2011).
[11] D. Fu, M. Itoh, S.-y. Koshihara, T. Kosugi, and S. Tsuneyuki, Phys. Rev. Lett. **100**, 227601 (2008).
[12] D. Hennings, A. Schnell, and G. Simon, J. Am. Ceram. Soc. **65**, 539 (1982).
[13] P. Hohenberg and W. Kohn, Phys. Rev. **136**, B864 (1964).
[14] B. J. Campbell, H. T. Stokes, D. E. Tanner, and D. M. Hatch, J. Appl. Crystallogr. **39**, 607 (2006).
[15] D. Orobengoa, C. Capillas, M. I. Aroyo, and J. M. Perez-Mato, J. Appl. Crystallogr. **42**, 820 (2009).
[16] J. M. Perez-Mato, D. Orobengoa, and M. I. Aroyo, Acta Crystallogr., Sect. A: Found. Crystallogr. **66**, 558 (2010).
[17] J. Tolédano and P. Tolédano, *The Landau Theory of Phase Transitions* (World Scientific, Singapore, 1987).
[18] H. T. Stokes, D. M. Hatch, and H. M. Nelson, Phys. Rev. B **47**, 9080 (1993).
[19] P. V. Balachandran, J. Theiler, J. M. Rondinelli, and T. Lookman, Sci. Rep. **5**, 13285 (2015).
[20] P. V. Balachandran, N. A. Benedek, and J. M. Rondinelli, in *Information Science for Materials Discovery and Design*, edited by T. Lookman, F. J. Alexander, and K. Rajan, Springer Series in Materials Science, Vol. 225 (Springer International, Switzerland, 2016), pp. 213–222.
[21] V. Vapnik, *The Nature of Statistical Learning Theory* (Springer, New York, 2000).
[22] A. J. Smola and B. Schölkopf, Stat. Comput. **14**, 199 (2004).
[23] A. Karatzoglou, D. Meyer, and K. Hornik, J. Stat. Software **15**, 1 (2006).
[24] See Supplemental Material at http://link.aps.org/supplemental/10.1103/PhysRevB.93.144111 for details.
[25] J. Qi, Z. Gui, W. Li, Y. Wang, Y. Wu, and L. Li, Mater. Lett. **56**, 507 (2002).
[26] S. C. Abrahams, S. K. Kurtz, and P. B. Jamieson, Phys. Rev. **172**, 551 (1968).
[27] J. P. Perdew, A. Ruzsinszky, G. I. Csonka, O. A. Vydrov, G. E. Scuseria, L. A. Constantin, X. Zhou, and K. Burke, Phys. Rev. Lett. **100**, 136406 (2008).
[28] P. Giannozzi, S. Baroni, N. Bonini, M. Calandra, R. Car, C. Cavazzoni, D. Ceresoli, G. L. Chiarotti, M. Cococcioni, I. Dabo, A. Dal Corso, S. de Gironcoli, S. Fabris, G. Fratesi, R. Gebauer, U. Gerstmann, C. Gougoussis, A. Kokalj, M. Lazzeri, L. Martin-Samos, N. Marzari, F. Mauri, R. Mazzarello, S. Paolini, A. Pasquarello, L. Paulatto, C. Sbraccia, S. Scandolo, G. Sclauzero, A. P. Seitsonen, A. Smogunov, P. Umari, and R. M. Wentzcovitch, J. Phys.: Condens. Matter **21**, 395502 (2009).
[29] D. Vanderbilt, Phys. Rev. B **41**, 7892 (1990).
[30] N. Troullier and J. L. Martins, Phys. Rev. B **43**, 1993 (1991).
[31] H. J. Monkhorst and J. D. Pack, Phys. Rev. B **13**, 5188 (1976).
[32] H. T. Stokes and D. M. Hatch, J. Appl. Crystallogr. **38**, 237 (2005).
[33] K. Momma and F. Izumi, J. Appl. Crystallogr. **41**, 653 (2008).
[34] S. Baroni, S. de Gironcoli, A. Dal Corso, and P. Giannozzi, Rev. Mod. Phys. **73**, 515 (2001).
[35] K. Kunc and R. M. Martin, Phys. Rev. Lett. **48**, 406 (1982).
[36] A. Togo, F. Oba, and I. Tanaka, Phys. Rev. B **78**, 134106 (2008).
[37] D. Meyer, E. Dimitriadou, K. Hornik, A. Weingessel, and F. Leisch, e1071: Misc Functions of the Department of Statistics, Probability Theory Group (Formerly: E1071), TU Wien (2015), R package version 1.6-7.

[38] R Core Team, *R: A Language and Environment for Statistical Computing* (R Foundation for Statistical Computing, Vienna, Austria, 2012).
[39] D. P. MacKinnon, C. M. Lockwood, and J. Williams, Multivariate Behav. Res. **39**, 99 (2004).
[40] S. Tinte, M. G. Stachiotti, S. R. Phillpot, M. Sepliarsky, D. Wolf, and R. L. Migoni, J. Phys.: Condens. Matter **16**, 3495 (2004).
[41] T. A. Colson, M. J. Spencer, and I. Yarovsky, Comput. Mater. Sci. **34**, 157 (2005).
[42] J. M. Rondinelli, A. S. Eidelson, and N. A. Spaldin, Phys. Rev. B **79**, 205119 (2009).
[43] B. Kocsis, J. M. Perez-Mato, E. S. Tasci, G. de la Flor, and M. I. Aroyo, J. Appl. Crystallogr. **47**, 1165 (2014).
[44] A. García and D. Vanderbilt, Phys. Rev. B **54**, 3817 (1996).
[45] W. D. Parker, J. M. Rondinelli, and S. M. Nakhmanson, Phys. Rev. B **84**, 245126 (2011).
[46] A. Lebedev, Phys. Solid State **51**, 362 (2009).
[47] H. Moriwake, A. Kuwabara, C. A. J. Fisher, H. Taniguchi, M. Itoh, and I. Tanaka, Phys. Rev. B **84**, 104114 (2011).
[48] W. Jauch and A. Palmer, Phys. Rev. B **60**, 2961 (1999).
[49] R. H. Buttner and E. N. Maslen, Acta Crystallogr., Sect. B: Struct. Sci. **48**, 764 (1992).
[50] A. W. Hewat, Ferroelectrics **6**, 215 (1973).
[51] A. R. Akbarzadeh, I. Kornev, C. Malibert, L. Bellaiche, and J. M. Kiat, Phys. Rev. B **72**, 205104 (2005).
[52] A. Feteira, D. C. Sinclair, K. Z. Rajab, and M. T. Lanagan, J. Am. Ceram. Soc. **91**, 893 (2008).
[53] É. Bévillon, A. Chesnaud, Y. Wang, G. Dezanneau, and G. Geneste, J. Phys.: Condens. Matter **20**, 145217 (2008).
[54] J. W. Bennett, I. Grinberg, and A. M. Rappe, Phys. Rev. B **73**, 180102 (2006).
[55] L. Louis and S. M. Nakhmanson, Phys. Rev. B **91**, 134103 (2015).
[56] A. Bilić and J. D. Gale, Phys. Rev. B **79**, 174107 (2009).
[57] P. V. Balachandran and J. M. Rondinelli, Phys. Rev. B **88**, 054101 (2013).
[58] H. T. Stokes, B. J. Campbell, and R. Cordes, Acta Crystallogr., Sect. A: Found. Crystallogr. **69**, 388 (2013).
[59] M. A. Helal, T. Mori, and S. Kojima, Appl. Phys. Lett. **106**, 182904 (2015).
[60] P. V. Balachandran, S. R. Broderick, and K. Rajan, Proc. R. Soc. London, Ser. A **467**, 2271 (2011).
[61] M. Sindhu, N. Ahlawat, S. Sanghi, R. Kumari, and A. Agarwal, J. Alloys Compd. **575**, 109 (2013).
[62] V. Tiwari, D. Pandey, P. Krishna, R. Chakravarthy, and B. Dasannacharya, Phys. B (Amsterdam) **174**, 112 (1991).
[63] G. Laurita, K. Page, S. Suzuki, and R. Seshadri, Phys. Rev. B **92**, 214109 (2015).
[64] A. Belsky, M. Hellenbrandt, V. L. Karen, and P. Luksch, Acta Crystallogr., Sect. B: Struct. Sci. **58**, 364 (2002).
[65] L. Bunina and A. Kudzin, Fiz. Tverd. Tela **10**, 3156 (1968) [Sov. Phys. Solid State **10**, 2496 (1969)].
[66] M. Adachi, Y. Akishige, T. Asahi, K. Deguchi, K. Gesi, K. Hasebe, T. Hikita, T. Ikeda, Y. Iwata, M. Komukae, T. Mitsui, E. Nakamura, N. Nakatani, M. Okuyama, T. Osaka, A. Sakai, E. Sawaguchi, Y. Shiozaki, T. Takenaka, K. Toyoda, T. Tsukamoto, and T. Yagi, in *Oxides*, edited by Y. Shiozaki, E. Nakamura, and T. Mitsui, Landolt-Börnstein-Group III Condensed Matter Vol. 36A1 (Springer, Berlin, 2001), pp. 1–12.
[67] T. Qi, I. Grinberg, and A. M. Rappe, Phys. Rev. B **82**, 134113 (2010).
[68] J. C. Wojdeł and J. Íñiguez, Phys. Rev. B **90**, 014105 (2014).
[69] Y. J. Shan, H. Mori, R. Wang, W. Luan, H. Imoto, Mitsuruitoh, and T. Nakamura, Ferroelectrics **259**, 85 (2001).
[70] B. J. Kennedy, Q. Zhou, and M. Avdeev, J. Solid State Chem. **184**, 2987 (2011).
[71] V. M. Goldschmidt, Die Naturwissenschaften **14**, 477 (1926).
[72] L. Pauling, *The Chemical Bond* (Cornell University Press, Ithaca, New York, 1967).
[73] R. D. Shannon, Acta Crystallogr., Sect. A: Found. Crystallogr. **32**, 751 (1976).
[74] S. Suzuki, A. Honda, N. Iwaji, S. Higai, A. Ando, H. Takagi, H. Kasatani, and K. Deguchi, Phys. Rev. B **86**, 060102 (2012).
[75] S. Suzuki, T. Takeda, A. Ando, and H. Takagi, Appl. Phys. Lett. **96**, 132903 (2010).
[76] T. Lookman, P. V. Balachandran, D. Xue, G. Pilania, T. Shearman, J. Theiler, J. Gubernatis, J. Hogden, K. Barros, E. BenNaim, and F. Alexander, in *Information Science for Materials Discovery and Design*, edited by T. Lookman, F. J. Alexander, and K. Rajan, Springer Series in Materials Science Vol. 225 (Springer International, Switzerland, 2016), pp. 3–12.
[77] P. V. Balachandran, D. Xue, J. Theiler, J. Hogden, and T. Lookman, Sci. Rep. **6**, 19660 (2016).